

Herbig Stars' Near-Infrared Excess: An Origin in the Protostellar Disk's Magnetically-Supported Atmosphere

N. J. Turner^{1,2}, M. Benisty^{2,3}, C. P. Dullemond^{2,4} and S. Hirose⁵

ABSTRACT

Young stars with masses 2–8 Suns, called the Herbig Ae and Be stars, often show a near-infrared excess too large to explain with a hydrostatically-supported circumstellar disk of gas and dust. At the same time the accretion flow carrying the circumstellar gas to the star is thought to be driven by magneto-rotational turbulence, which according to numerical MHD modeling yields an extended low-density atmosphere supported by the magnetic fields. We demonstrate that the base of the atmosphere can be optically-thick to the starlight and that the parts lying near 1 AU are tall enough to double the fraction of the stellar luminosity reprocessed into the near-infrared. We generate synthetic spectral energy distributions (SEDs) using Monte Carlo radiative transfer calculations with opacities for sub-micron silicate and carbonaceous grains. The synthetic SEDs closely follow the median Herbig SED constructed recently by Mulders and Dominik, and in particular match the large near-infrared flux, provided the grains have a mass fraction close to interstellar near the disk's inner rim.

Subject headings: protoplanetary disks — radiative transfer

¹Jet Propulsion Laboratory, California Institute of Technology, Pasadena, California 91109, USA; neal.turner@jpl.nasa.gov

²Max-Planck-Institut für Astronomie, Königstuhl 17, D-69117 Heidelberg, Germany

³Observatoire de Grenoble, Université Joseph Fourier, Grenoble, France

⁴Institut für Theoretische Astrophysik, Zentrum für Astronomie, Universität Heidelberg, Albert-Ueberle-Str. 2, 69120 Heidelberg, Germany

⁵Institute for Research on Earth Evolution, Japan Agency for Marine-Earth Science and Technology, 3173-25 Showamachi, Kanazawa-ku, Yokohama, Kanagawa 236-0001, Japan

1. INTRODUCTION

Young intermediate-mass stars with disks commonly show a large near-infrared excess at wavelengths 2–4 μm . The luminosity in the excess is often a noticeable fraction of the stellar bolometric luminosity. Hydrostatic disk models fail to reproduce the near-infrared flux, emitting too little by a factor two for some stars (Vinković et al. 2006). This is a puzzle because in the basic hydrostatic picture each star is allowed only a narrow range of fluxes, determined as follows (Dullemond & Monnier 2010): the 2- μm emission arises in material with temperatures near the silicate sublimation threshold of about 1500 K. Such temperatures occur at a certain distance from the star, inside which the dust cannot survive, leaving the disk optically-thin. The material at the sublimation front therefore faces the star directly, intercepting and re-emitting at 2 μm a fraction of the stellar luminosity equal to the ratio of the disk thickness to the front’s radius. The disk’s density scale height in hydrostatic balance is proportional to the sound speed divided by the orbital frequency, two quantities that both are fixed — the sound speed by the sublimation temperature, and the orbital frequency by the radius where the sublimation temperature is reached. Varying the grain size and composition shifts the sublimation front somewhat, but the ratio of density scale height to sublimation radius changes little. For purposes of the near-infrared excess, the disk’s thickness is equal to the height of the surface where the starlight is absorbed and reprocessed. This starlight-absorbing surface lies a few density scale heights from the equatorial plane, growing logarithmically with the surface density owing to the steep density profile of the hydrostatic disk atmosphere. In quite a few objects, the near-infrared excess cannot be accounted for even with extreme disk masses.

The puzzle only grows stronger when longer infrared wavelengths are considered. Matching the excess at 7 μm and the 13.5-to-7- μm flux ratio requires artificially scaling up the disk’s thickness near 1 AU by factors of as much as three compared with hydrostatic models, in the sample of 33 Herbig stars examined by Acke et al. (2009).

Two main ideas have been proposed to explain the large near-infrared excesses. The first is that the disk is thicker because it is hot. The extra heating might come from accretion. Herbig systems’ $\text{H}\alpha$ equivalent widths, a measure of the accretion luminosity, correlate with the ratio of the K-band excess flux to that in the H-band, suggesting a link between accretion and the inner disk shape (Manoj et al. 2006). However as Manoj et al. were aware, the accretion power by itself cannot explain the observed near-infrared fluxes without mass flow rates exceeding $10^{-6} M_{\odot} \text{ yr}^{-1}$ (Hillenbrand et al. 1992; Lada & Adams 1992). Yet the flow rate must be less than $10^{-7} M_{\odot} \text{ yr}^{-1}$ for the gas inside the silicate sublimation radius to be optically thin (Hartmann et al. 1993) and compatible with the central holes detected in near-infrared interferometric observations of many Herbig stars. The holes have sizes

generally consistent with the sublimation radius over a broad range of stellar luminosities, as reviewed by Dullemond & Monnier (2010). Alternatively, the extra heating might come from fast-moving electrons ejected from the grains by stellar ultraviolet photons. At the low gas densities found in the hydrostatic atmosphere, heat transfer from gas to dust is inefficient. The photoelectron-heated gas cannot easily cool, and reaches temperatures up to several thousand degrees (Thi et al. 2011). However the low gas densities also mean that even sub-micron grains quickly settle out, so the hot material is likely to be transparent to the starlight.

The other main idea is an extra system component that is warm enough to emit significantly in the near-infrared, such as a spherical halo or envelope (Hartmann et al. 1993; Vinković et al. 2006), dusty disk wind (Vinković & Jurkić 2007; Bans & Königl 2012) or cloud of dust ejected by magnetic forces (Ke et al. 2012). A component covering a large solid angle might help account for the common occurrence of variable circumstellar extinction among the Herbig Ae stars (Bibo & The 1991; Malfait et al. 1998; Natta et al. 2000) and especially the members of the UX Ori class (Grinin et al. 1998, 2009). However spherical structures by themselves appear incompatible with interferometric measurements (Tuthill et al. 2001; Eisner et al. 2004). Combining a spherical halo of modest optical depth with a hydrostatic disk yields a better fit than either component alone in several cases (Monnier et al. 2006; Verhoeff et al. 2011; Chen et al. 2012).

Here we focus on the expectation that the accretion stresses in the sufficiently-ionized parts of the disks come from magnetic forces (Umebayashi & Nakano 1988; Balbus & Hawley 1991; Gammie 1996; Zhu et al. 2009; Armitage 2011). A magnetically-supported atmosphere is a natural consequence, since shearing-box MHD calculations extending more than a few scale heights from the midplane show magnetic fields generated in magneto-rotational turbulence and rising buoyantly to form an atmosphere in which magnetic pressure exceeds gas pressure (Miller & Stone 2000; Flaig et al. 2010). The atmosphere is optically-thin to its own continuum emission when its base is set by the penetration of the young star’s ionizing X-ray photons (Bai & Goodman 2009), but is nevertheless optically-thick to the starlight which illuminates the disks around low-mass T Tauri stars at grazing incidence (Hirose & Turner 2011).

In this contribution we demonstrate that the magnetically-supported atmosphere is optically-thick to the starlight in Herbig disks too. The magnetic support can make the inner disk two to three times taller, so that it intercepts and reprocesses into the near-infrared a correspondingly greater fraction of the stellar luminosity.

Our model star is described in section 2 and the disk supported jointly by gas and magnetic pressure in section 3. After choosing dust opacity curves (section 4) we use a Monte

Carlo radiative transfer approach (section 5) to compute the disk’s shape and temperature, solving jointly for global radiative and vertical magneto-hydrostatic equilibrium (section 6). Synthetic observations are made using the ray-tracing method described in section 7. The results are set out in section 8 and the summary and conclusions follow in section 9.

2. STAR

Our star is a $2.4\text{-}M_{\odot}$ Herbig Ae modeled on AB Aurigae. Its radius $2.55R_{\odot}$ and temperature 9550 K yield luminosity $47.9 L_{\odot}$ (van den Ancker et al. 1998). The star emits the spectrum of the Solar-metallity Kurucz model with the nearest gravity and effective temperature — 10^4 cm s^{-2} and 9500 K.

3. DISK

We assume the surface density Σ falls inversely with radius r until cut off exponentially at outer radius r_o :

$$\Sigma = \frac{M_d}{2\pi r_o^2} \left(\frac{r_o}{r} \right) \exp(-r/r_o). \quad (1)$$

This is a similarity solution with total mass M_d , obtained under a simple viscosity prescription (Hartmann et al. 1998). Eq. 1 also is a fair match to the surface densities measured at separations of tens of AU using millimeter interferometry of the dust continuum emission from T Tauri stars (Andrews et al. 2010). We set the outer cutoff radius to $r_o = 250 \text{ AU}$. In addition we cut the disk short inside a radius r_i . This is meant to model not the stellar magnetosphere’s truncation of the gas, but the sublimation front’s truncation of the optical depth. Directly solving for the position of the front can introduce convergence issues (Kama et al. 2009) which we wish to avoid. Inside r_i we roll off the surface density by the factor $\exp[-(\{r - r_i\}/\Delta r_i)^2]$. The inner cutoff radius and scale length are $r_i = 0.7$ and $\Delta r_i = 0.1 \text{ AU}$. With these choices the disk is optically-thin inside about 0.4 AU which is near the expected sublimation radius for our model star. We check after the fact that the temperature at unit radial optical depth is close to the sublimation threshold. Solving in detail for the shape of the sublimation front is unlikely to significantly reduce the fraction of the starlight intercepted by the disk within 1 AU, but could change how the reprocessed luminosity is distributed across near-infrared wavelengths. The surface density is 1000 g cm^{-2} at 1 AU, yielding a total disk mass $0.176M_{\odot}$ or 7% of the stellar mass. The surface density profile, shown in figure 1, along with the temperatures found as described below, yields a Toomre Q parameter that is smallest near 160 AU, where it exceeds seven in all models,

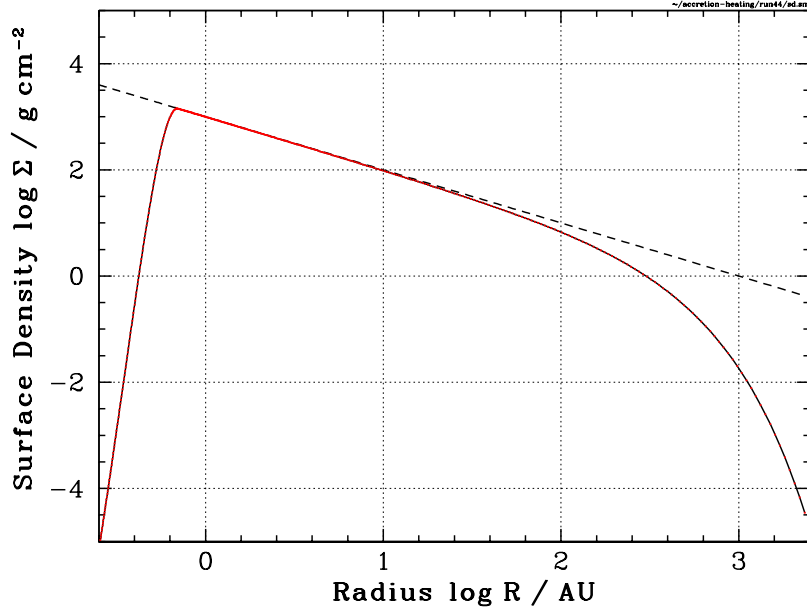


Fig. 1.— Surface density profile in the model Herbig disks (solid curve). The radiative transfer grid cells’ radial edges are marked by tiny red squares. The dashed black diagonal line shows a $1/r$ dependence.

indicating stability against self-gravity.

The vertical profile of density in each disk annulus is obtained as follows. First, we fit the mean density profile in the fiducial radiation-MHD calculation from Hirose & Turner (2011) with the sum of a gas-pressure-supported isothermal interior and a magnetically-supported atmosphere (figure 2). The interior has a Gaussian density profile in the height z , while the atmosphere is exponential:

$$\frac{\rho(z)}{\rho_0} = \exp\left(-\frac{z^2}{2H^2}\right) + \frac{1}{78.6} \exp\left(-\frac{z}{1.57H}\right), \quad (2)$$

where ρ_0 is the Gaussian’s midplane density, $H = c_s(z=0)/\Omega$ the density scale height, Ω the Keplerian orbital frequency and $c_s(z=0)$ the midplane isothermal sound speed, computed using the gas mean molecular weight 2.3.

In the Monte Carlo radiative transfer calculations we use H to rescale the MHD results which Hirose & Turner (2011) obtained 1 AU from an $0.5\text{-}M_\odot$ T Tauri star. To be conservative we round down the exponential scale length and normalization, making the magnetically-supported atmosphere a little more compact and lower-mass. We adopt the

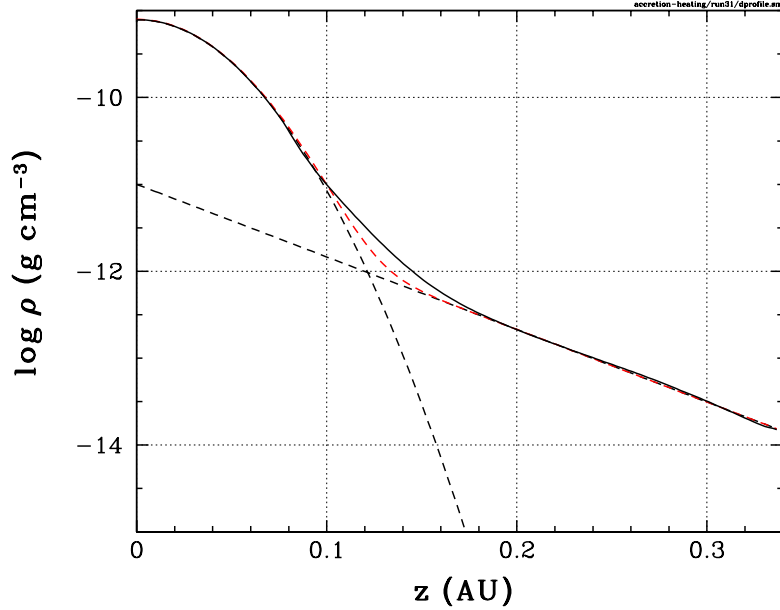


Fig. 2.— Mean density profile in the shearing-box radiation-MHD calculation of Hirose & Turner (2011) (solid black line). The profile is fit by summing two components, a Gaussian and an exponential (eq. 2; dashed black lines) with the total shown by a dashed red curve. The fit is good except near the transition between the components, where the MHD result is up to 60% denser.

density profile

$$\rho(z) = \rho_{HSE}(z) + N\rho_0 \exp\left(-\frac{z}{AH}\right), \quad (3)$$

where ρ_{HSE} is the profile obtained by solving for vertical hydrostatic balance while fixing the variation of the temperature with mass column to the profile found in the previous Monte Carlo transfer iteration. The parameters are $N = 1/80$, which normalizes the exponential relative to the Gaussian, and $A = 1.5$, the exponential scale height in units of H . The hydrostatic component’s midplane density $\rho_0 = \rho_{HSE}(0)$ is chosen using simple root-finding by bisection, so that the total profile has the desired surface density.

We now consider three configurations: (A) the entire disk is supported in the traditional fashion by gas pressure alone, (B) gas and magnetic pressures contribute throughout according to eq. 3, and (C) magnetic pressure adds to gas pressure only in annuli with a narrow range of radii just outside the silicate sublimation front, where the high temperatures ensure good magnetic coupling through collisional ionization of the alkali metals. The three configurations are listed in table 1. The magnetically-supported “bump” in the third con-

figuration is merged smoothly with the surrounding gas-pressure-supported disk by giving the exponential atmosphere’s scale height a Gaussian radial variation about the maximum value $A(r_b) = 1.5$. The Gaussian’s FWHM is equal to the radius r_b of the bump’s peak.

The atmosphere’s thickness likely also depends on the net vertical magnetic flux, which is a product of the global transport of magnetic fields. Given the uncertainties regarding this transport, we here simply fix the atmosphere’s scale height in units of the gas pressure scale height to a value similar to that found by Hirose & Turner (2011). Their radiation-MHD calculations have a net vertical magnetic flux with pressure 3×10^5 times less than the midplane gas pressure.

4. DUST OPACITY

The disks’ opacity comes primarily from dust, which we assume is well-mixed in the gas except where otherwise specified. We adopt opacities from Preibisch et al. (1993) who matched Mie calculations of dust particles’ optical response against data from molecular clouds. The grain model consists of silicate and carbonaceous particles, each with a power-law size distribution of exponent -3.5 . The minimum and maximum sizes are 0.04 and $1 \mu\text{m}$ for the silicate particles and 0.007 and $0.03 \mu\text{m}$ for the carbon particles. The opacity curves are shown in figure 3 together with the albedos, or ratios of scattering to total opacity. Scattering contributes about half of the total cross-section at optical wavelengths, and is assumed isotropic.

SED modeling suggests dust is depleted in T Tauri disk atmospheres by factors 10 – 10^4 compared with the interstellar medium (Furlan et al. 2006, 2009). A gas-to-dust ratio of 12800 , in the same range, appears to be needed to understand the water emission from T Tauri stars (Meijerink et al. 2009). Furthermore, planet formation requires incorporating

Table 1. The three disk configurations’ support against vertical gravity.

Name	Gas Support	Magnetic Support
Gas	Yes	None
Magnetic	Yes	Throughout
Magnetic bump	Yes	Only in bump near inner rim ^a

^aThe bump is centered $r_b = 1$ AU from the star.

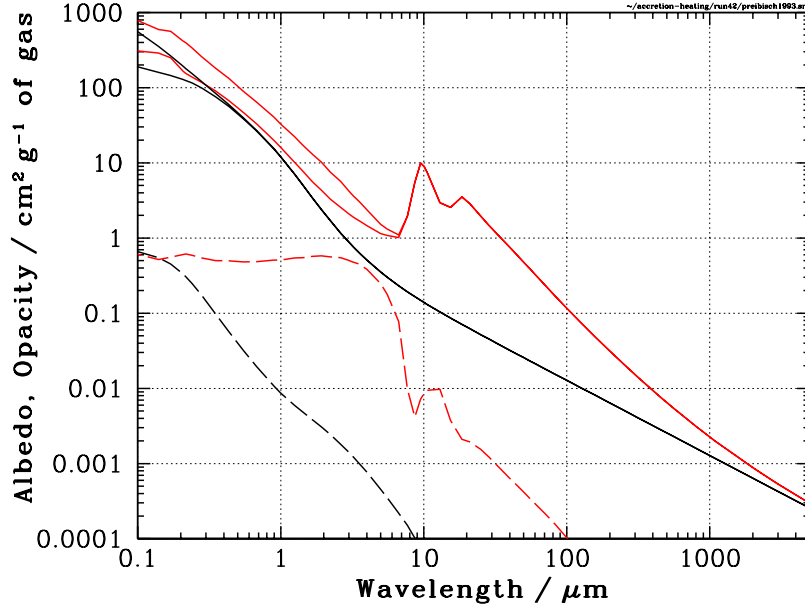


Fig. 3.— Wavelength dependence of the opacities for the silicate and carbon particles (red) and for the carbon particles alone (black) from Preibisch et al. (1993). The lower in each pair of solid curves is the absorption opacity, the upper the sum of absorption and scattering opacities. Dashed curves indicate the corresponding albedos. The two black solid curves nearly coincide due to the carbon particles’ low albedos.

some of the solid material into bigger bodies. We therefore consider two dust-to-gas mass ratios: the nominal interstellar value, as shown in figure 3, and a hundredfold depletion. The dust opacities are simply scaled down by the depletion factor ϵ . Additionally we consider a scenario in which the dust takes the depleted abundance except in a ring around $r_r = 1$ AU, where the peak dust mass fraction matches that in the dusty scenario. The mass fraction is a Gaussian in radius, asymptoting to the depleted value far from the star. The three dust distributions are listed in table 2.

To summarize, each model disk is uniquely specified by listing the magnetic support from table 1 and the dust distribution from table 2. Since we consider three magnetic configurations and three dust scenarios, there are nine models in all.

5. RADIATION FIELD AND TEMPERATURE

We compute the radiative equilibrium temperatures by emitting a large number of photon packets from the star into the disk where they are scattered, absorbed and re-emitted as many times as needed till they escape to infinity. With this approach the energy is conserved exactly. The stellar luminosity is divided equally among the packets. We use the temperature relaxation procedure of Bjorkman & Wood (2001), drawing the frequencies of the re-emitted packets from the difference between the old and new emission spectra, such that the local radiation field adjusts to the updated temperature. The gas and dust are assumed to share a single temperature at each point. For efficiency when estimating the radiation absorption rates and the radiation’s mean intensity, we include the contributions from all along the packet paths (Lucy 1999). The intensity is accumulated in 20 contiguous non-overlapping wavelength bins including those centered on the photometric bands U, B, V, R, I, J, H and K, the four Spitzer IRAC channels at 3.6, 4.5, 5.8 and 8 μm , and the Spitzer MIPS 24- μm channel. For contiguous wavelength coverage these are rounded out with bands centered at wavelengths 1, 1.9, 2.79, 10, 12, 14.5 and 18 μm . The center of each intensity bin appears as an open circle on the spectral energy distributions in section 8.2 below.

We compute the temperatures neglecting accretion heating. Under magneto-rotational turbulence, much of the released gravitational energy is deposited in the disk atmosphere, at low optical depths to the disk’s own radiation (Bai & Goodman 2009; Hirose & Turner 2011). Heating at low optical depths has a reduced effect on the midplane temperatures. Also, the accretion heating falls off with radius faster than the stellar irradiation heating, so that including the accretion power would increase the disk’s thickness most near the inner rim. By neglecting the accretion heating we thus obtain a lower limit on the fraction of the stellar luminosity reprocessed into the infrared near the disk’s inner rim.

Table 2. The three dust distributions.

Name	Dust-to-Gas Mass Ratio, 0.01ϵ
Depleted	10^{-4} throughout
Dusty	10^{-2} throughout
Dusty ring ^a	$10^{-4} \times (1 + 99 \exp[-4\{r/r_r - 1\}^2])$

^aThe dusty ring is centered $r_r = 1$ AU from the star.

Because we neglect the accretion heating, the disk’s interior is isothermal on cylinders. We therefore save the expense of computing temperatures in the most optically-thick regions by simply bouncing back any packets reaching a certain mass column, chosen so the overlying material is optically thick at wavelengths near its thermal emission peak. The bouncing threshold is set to $30/\epsilon \text{ g cm}^{-2}$ in all the calculations shown here. We replace the missing interior temperatures by the mean of the last few well-sampled values above.

The disk is divided into a grid of $N = 800$ cells spanning the four decades in radius from $r_0 = 0.25$ to $r_N = 2500$ AU. The cells are concentrated near the inner rim to better resolve the transition from optically-thin to thick in the radial direction. Cell j ’s inner radius r_j is given by $\log(r_j/r_0) = C [(\Delta/C + 1)^{j/N} - 1]$, where $\Delta = 4$ is the log of the ratio of the grid’s outer to inner radius. We choose a concentration parameter $C = 0.3$. The strength of the concentration can be seen in figure 1, where dots mark the cell edges r_j . In the vertical direction the grid has 280 cells uniformly-spaced between the equatorial plane and height $z = 0.7r_j$, yielding a spacing 0.25% of the radius. This choice of upper boundary ensures all the material with starlight optical depth greater than 10^{-3} lies on the grid, even in the flared outer parts of our nine model disks.

6. JOINT RADIATIVE AND MAGNETO-HYDROSTATIC EQUILIBRIUM

Once new temperatures have been found through the Monte Carlo radiative transfer procedure, we restore vertical equilibrium by reconstructing the density profile within each disk annulus as in section 3, while holding fixed the surface density and the variation of the temperature with the mass column.

We iterate five times between radiative transfer and magneto-hydrostatic balancing. In each case the third, fourth and fifth iterations show only minor differences, indicating the solution is close to converged. Each iteration of the radiative transfer calculation involves 10^7 photon packets.

7. SYNTHETIC IMAGES AND SPECTRA

The procedure outlined above yields the density $\rho(r, z)$, temperature $T(r, z)$ and frequency-dependent mean radiation intensity $J_\nu(r, z)$. Note that J_ν is taken piecewise constant across each of the 20 wavebands described in section 5, the individual photon packets’ wavelengths having been discarded during the accumulation. From these three quantities we compute

synthetic images and spectra by solving the transfer equation,

$$\frac{dI_\nu}{d\tau_\nu} = I_\nu - \frac{\kappa_\nu B_\nu(T) + \sigma_\nu J_\nu}{\kappa_\nu + \sigma_\nu}, \quad (4)$$

on a grid of parallel rays extending toward the observer at infinity, following Yorke (1986). The symbols have their usual meanings (Mihalas 1978) with ν the frequency, I_ν the specific intensity, J_ν its angle average, τ_ν the optical depth and κ_ν and σ_ν the absorption and scattering opacities. The differential optical depth $d\tau_\nu$ over a step of length dl is $(\kappa_\nu + \sigma_\nu)\rho dl$.

Solving the transfer equation in this way is preferable over binning the Monte Carlo photon packets in angle as they emerge from the system, because it yields images with adequate spatial resolution using far fewer packets.

8. RESULTS

8.1. Does the Atmosphere Absorb Starlight?

The magnetically-supported atmosphere contains only a small fraction of the disk mass. A natural question to start with is therefore whether the atmosphere is optically-thick enough to affect the reprocessing of the starlight. In figure 4 we draw the surfaces of unit starlight optical depth in the nine models. The dust-depleted cases in the first panel show clear differences between versions with and without the magnetic support. The starlight-absorbing surface lies 1.75 times higher at 1 AU with magnetic support throughout (green dashed line) than in the hydrostatic version (blue dashed line). The ratio is 1.48 times for the magnetically-supported bump (red dashed line). The magnetic support’s effects are even stronger in the dusty cases (second panel) where the corresponding ratios are 3.07 and 2.82. The magnetic support makes the starlight-absorbing surface taller by similar factors in the cases with dusty inner rings (third panel) where the ratios to the hydrostatic version are 3.06 and 2.87. Furthermore, synthetic images of the central 2.5 AU show the magnetically-supported material noticeably alters the appearance in the near-infrared J, H and K bands (figure 5), increasing the surface area of bright material lying within 1 AU. Considering all six scenarios with magnetic support, clearly the atmosphere reprocesses significant stellar luminosity beyond that intercepted by the hydrostatic models.

Closer examination shows a striking correspondence between the surface brightness in fig. 5 and the slope of the starlight-absorbing surface in fig. 4. In particular, the brightest of the three dusty models just inside 1 AU is the magnetically-supported bump, which has its surface tilted most steeply toward the star.

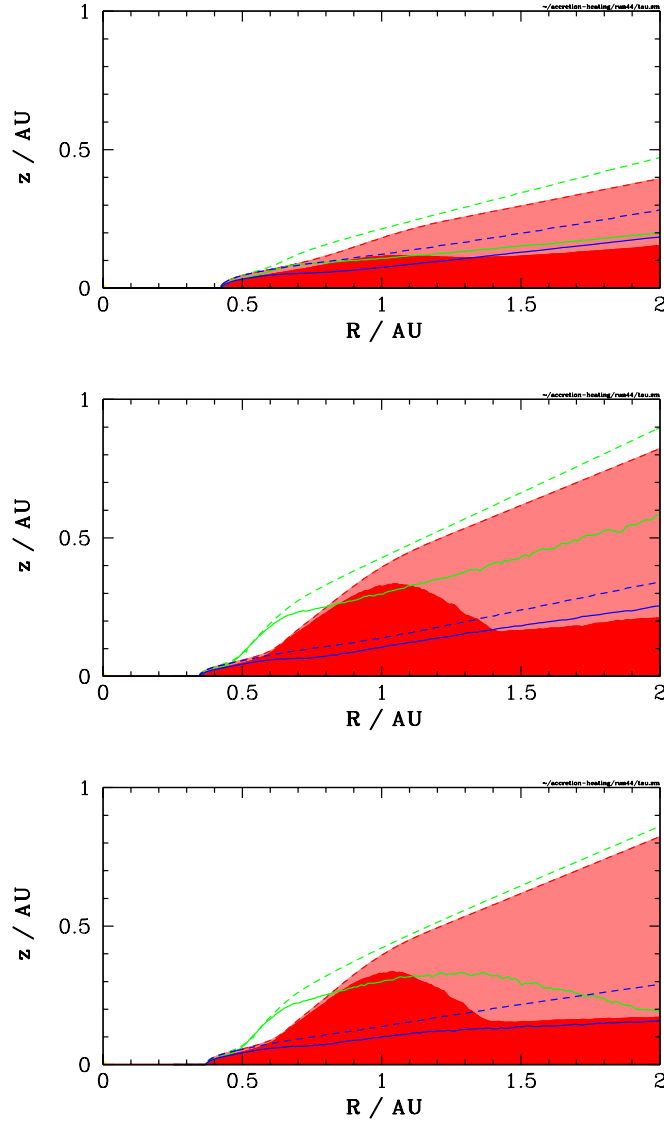


Fig. 4.— Surfaces of unit optical depth for starlight entering the nine model disks. The wavelength is $0.314 \mu\text{m}$, near the starlight peak. The three dust-depleted disks are at top, the three dusty disks at center and the three disks with dusty rings below. In each panel the disk with gas support only is shown by blue lines, the disk with magnetic support throughout by green lines and the disk with the magnetically-supported bump by red lines and shading. In each case the upper dashed curve is the surface of unit optical depth for photons arriving from the star, while the lower solid curve is the surface of unit optical depth for photons traveling vertically downward. The yellow dot at the origin is the star to scale.

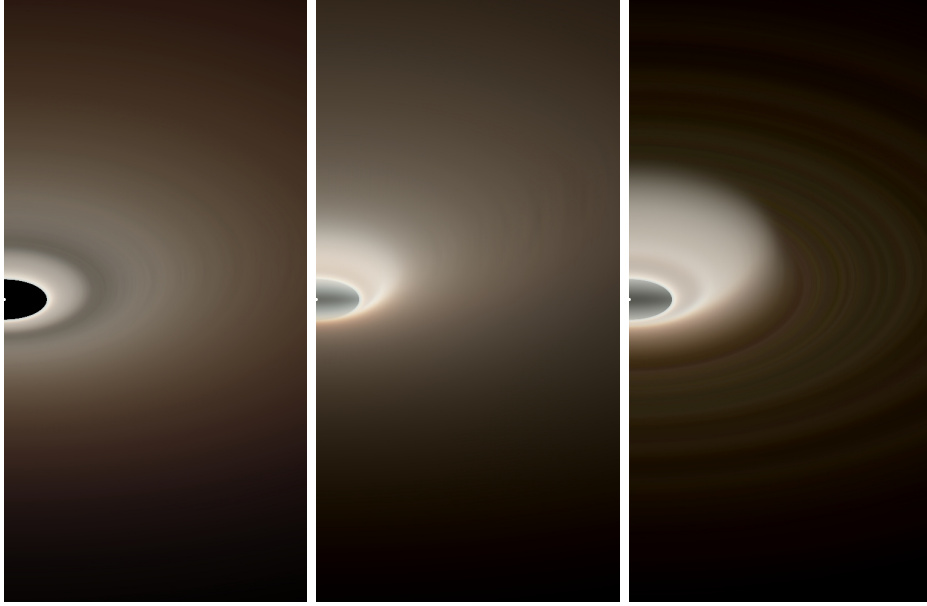


Fig. 5.— Synthetic images of the central region of the dusty Herbig disk with (left to right) no magnetic support, magnetic support throughout, and a magnetically-supported bump. The field of view is 2.5 AU wide and the system is inclined 60° from face-on. The star is shown to scale at the center of each panel’s left edge. The blue, green and red channels in each image correspond to wavelengths 1.25, 1.6 and $2.2 \mu\text{m}$ or J, H and K bands, respectively. A shared logarithmic intensity scale is used in all three panels.

Part of the extra height in the models with magnetically-supported atmospheres comes directly from the magnetic support. Another part comes from a secondary effect: since the atmosphere intercepts more starlight, the interior is hotter than in the hydrostatic models, and the gas pressure scale height is greater. The higher midplane temperatures near 1 AU resulting from magnetic support can be seen in figure 6. On the other hand, the magnetically-supported bump casts a shadow that appears as a dip in the temperature profiles at distances of several AU. Even the hydrostatic model has a shadow when the dust abundance is greatest in a ring near the disk’s inner edge (figure 6 bottom panel, blue curve). Starlight grazing the top of the dusty ring subsequently passes through less-opaque material, reaching unit optical depth only near 4 AU.

8.2. Is the System Bright Enough at Near-Infrared Wavelengths?

We wish to know whether the magnetic support increases the near-infrared excess enough to account for the observed SEDs. From the three spectral energy distributions

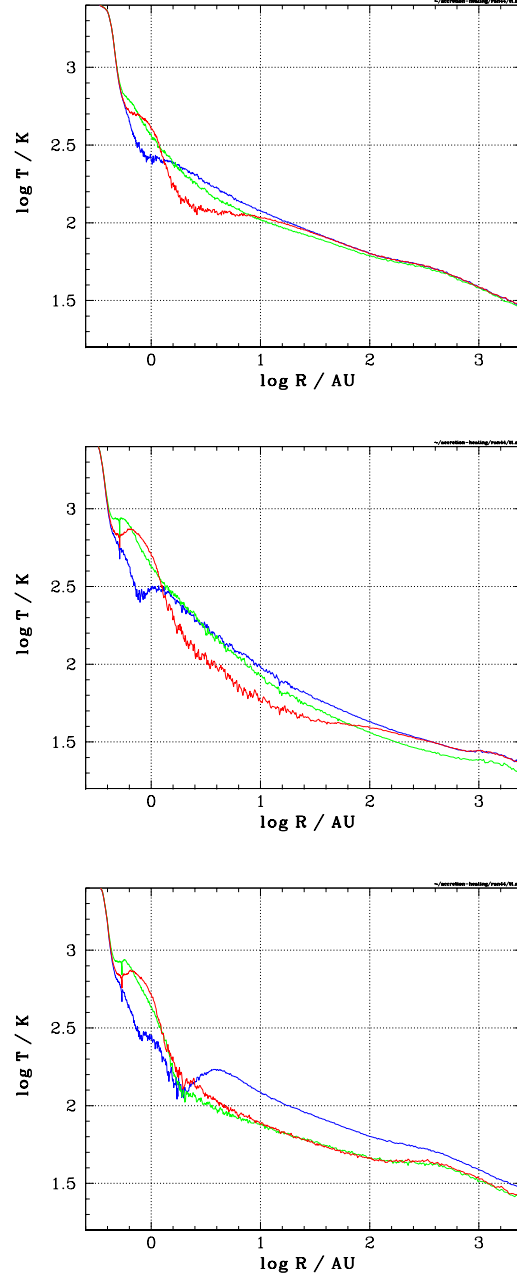


Fig. 6.— Midplane temperature vs. radius in the nine model disks. The dust-depleted disks are in the top panel, the dusty disks at center and the disks with dusty rings below. Colors are as in figure 4: blue shows the disk with gas support only, green the disk with magnetic support throughout and red the disk with the magnetically-supported bump.

in the first panel of figure 7, we see that all the dust-depleted models are too faint at wavelengths 2–4 μm by factors of two or more relative to the median Herbig system. Similar problems afflict the hydrostatic models that are dusty throughout, as well as those that are dusty only in a central ring (blue curves in second and third panels). By contrast, the versions with magnetic support lie close to the median SED at near-infrared wavelengths (green and red curves). Considering all nine models together, we see that four exceed the median observed near-infrared excess. All four have, just outside the sublimation radius, both a magnetized atmosphere and a near-interstellar dust-to-gas mass ratio. The key to reprocessing the extra starlight is a sufficient column of dust in the atmosphere, so lower dust-to-gas ratios would allow a similar outcome if the disk contained more gas than our chosen model (figure 1). With enough dust present, the magnetic support readily accounts for the excess that is missing from hydrostatic models.

The magnetically-supported models all do a poor job of matching the 10- μm silicate feature’s steep short-wavelength side. The most likely reason is an incorrect shape for the starlight-absorbing surface, due to the simple choices we made for the profiles of surface density and magnetic support. The disk annuli near 0.5 AU do show synthetic spectra with suitably steep slopes from 6–10 μm , suggesting that the median silicate band shape might be better matched with a shorter magnetically-supported bump placed nearer the star. A further possibility is that typical Herbig disks’ opacities have a wavelength dependence differing from the curves we used. Testing these ideas is a challenge for the future. Each calculation takes about a week of computer time and many parameters remain to be varied.

At wavelengths beyond 15 μm , the flux and SED slope are affected by the shape of the disk surface at and outside 10 AU. Magnetic support generally means more starlight intercepted near 1 AU and less outside 10 AU, making the outer annuli cooler and leading to steeper declines in flux with wavelength. The anti-correlation between the 7- μm excess and the 13.5-to-7- μm flux ratio observed by Acke et al. (2009) can thus qualitatively be explained by a variation from one system to the next in the strength of the magnetic support.

On the near-infrared bump’s other side, from 2 μm shortward, there is interferometric evidence for emission arising within the sublimation radius in some systems (Eisner et al. 2007; Isella et al. 2008; Benisty et al. 2010; Eisner et al. 2010). Our radiative transfer modeling does not address this component of the system. However if, as we propose, the near-infrared bump arises in material supported by the same magnetic fields that drive accretion, then correlations might be expected between the bump’s height, the surface density of the material within the sublimation radius, and the accretion signatures such as $\text{H}\alpha$ emitted near the stellar photosphere. Simultaneous optical and infrared observations could help illuminate such a connection.

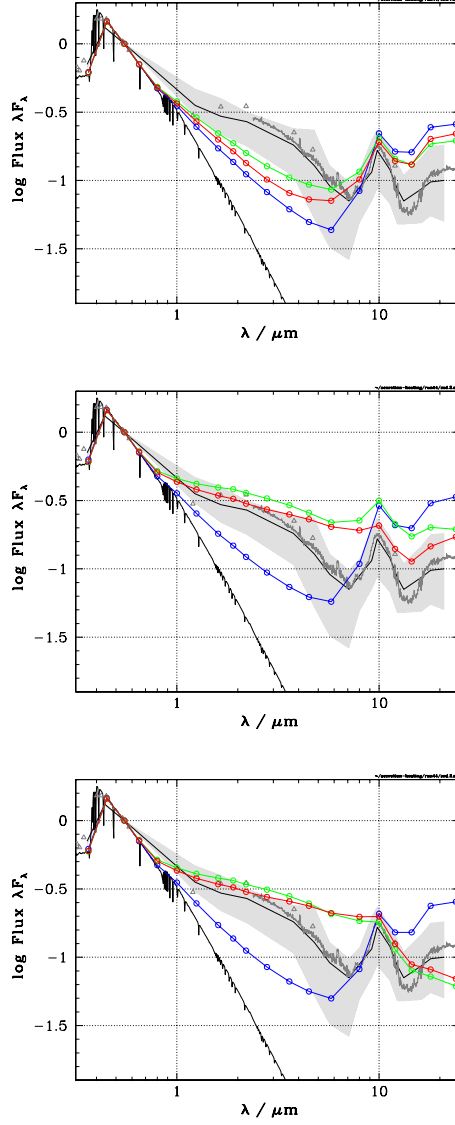


Fig. 7.— Spectral energy distributions of the nine model Herbig systems. The dust-depleted disks are at top, the dusty disks at center and the disks with dusty rings below. In each panel the lines' colors are as in figure 4: blue is the disk with gas support only, green the disk with magnetic support throughout and red the disk with the magnetically-supported bump. The thin black line indicates the stellar spectrum, a Kurucz model. The thick black line marking the median Herbig SED falls in a light-gray band reaching from the first to the third quartile (Mulders & Dominik 2012). The dark grey curve and triangles indicate a spectrum and photometry of the star AB Aurigae. All are normalized at $0.55 \mu\text{m}$.

8.3. Can Grains Remain Suspended in the Atmosphere?

We have assumed the grains providing the opacity are well-mixed in the gas. This is valid if the grains are stirred up, either by the turbulence or by the magnetic buoyancy, faster than they settle.

Magneto-rotational turbulence can loft material no quicker than the velocity correlation timescale, which is a fraction of the orbital period (Fromang & Papaloizou 2006). The linear magneto-rotational instability is slow-growing or stabilized high in the atmosphere, where the plasma beta is less than unity (Kim & Ostriker 2000). Even so, in non-linear stratified shearing-box MHD calculations the velocity dispersion remains large at these heights (Miller & Stone 2000; Flaig et al. 2010; Okuzumi & Hirose 2011). However out of an abundance of caution we set the stirring timescale to the slower magnetic buoyancy timescale, measured using the “butterfly” pattern visible when the magnetic pressure is plotted versus height and time. In shearing-box calculations this timescale is around ten orbits, with or without a dead zone (Miller & Stone 2000; Flaig et al. 2010; Hirose & Turner 2011). The upshot is that the grains repopulate the atmosphere within ten orbits if sufficiently coupled to the gas.

On the other hand, settling removes grains from the atmosphere with a speed such that the drag force balances the vertical component of the star’s gravity. The drag force is in the Epstein regime where the gas molecules’ mean free path exceeds the grain size. The settling time is the distance to the midplane divided by the settling speed and for compact spherical particles is given by

$$\frac{t_{\text{sett}}}{t_K} = \frac{1}{4\pi^2} \frac{t_K}{t_{\text{drag}}}, \quad (5)$$

where t_K is the Keplerian orbital period, and the drag stopping time $t_{\text{drag}} = \rho_d a / (\rho c_s)$ depends on the grains’ internal density ρ_d and radius a using the notation from Turner et al. (2010).

Now the grains to be concerned with are those that absorb the starlight and give off the disk inner rim’s thermal infrared emission. The starlight peaks near wavelength $0.3 \mu\text{m}$, the infrared emission near $3 \mu\text{m}$. The biggest contribution to the opacity is from grains with circumference comparable to the wavelength (van de Hulst 1957). Most important for the starlight opacity are thus grains smaller than $a = 0.1 \mu\text{m}$, and for the infrared opacity grains around $0.5 \mu\text{m}$ in radius. In discussing the settling of these particles we take an internal density $\rho_d = 3 \text{ g cm}^{-3}$, similar to that of terrestrial basalt. Densities are less for carbon-rich grains.

On the top panel of figure 8 we show by dotted lines the height to which the $0.1\text{-}\mu\text{m}$

grains settle within ten orbits. The settling heights are overlaid on the surfaces of unit direct starlight optical depth for the dusty models from figure 4. We see that settling is important only in the uppermost reaches of the atmosphere. For each of the three disk configurations, the dotted line lies above the unit-optical-depth curve on the part of the disk most directly facing the star. If settling were to remove all grains above the dotted line, an unlikely prospect, the height of the starlight-absorbing surface at 2 AU would be reduced about 11% in the hydrostatic disk, 27% in the disk with magnetic support throughout and 10% in the disk with the magnetically-supported bump. Note that the starlight-absorbing height beyond the bump is determined by the optically-thick bump itself. Furthermore, the settling would be unimportant right up to the starlight-absorbing surface in all the models if the inner disk had gas surface densities a few times greater than we have assumed.

The situation for the largest grains contributing to the opacity curves is shown in figure 8 bottom panel. Particles $1\ \mu\text{m}$ in radius settle significantly only in gas lying well above the $3\text{-}\mu\text{m}$ photosphere.

The dusty models shown in figure 8 impose the most severe settling constraint because their high opacity means the starlight is absorbed in gas with the lowest density. In the corresponding plots for the three dust-depleted disks, not shown, the starlight-absorbing surface falls well below the height where settling begins to matter. We conclude that the grains contributing most to the starlight opacity in our model disks are never more than marginally affected by settling, while the grains important for the thermal emission are unaffected.

The Lorentz force plays a minor role in the grains’ movements even in the disk with magnetic support throughout. Consider a grain traveling at its settling speed through a magnetic field with pressure ten times the local gas pressure. Struck by electrons from the surrounding plasma, the grain charges to the Coulomb limit in which the electric repulsion reduces the cross-section for colliding with further electrons to the point where the grain receives electrons and slower-moving ions at equal rates. The mutual electric potential between the grain and an electron approaching its surface is then about three times the thermal energy, as we determine by solving Okuzumi (2009) eq. 35. Grains $0.1\ \mu\text{m}$ in radius near the silicate sublimation front charge to about 20 electrons. Under these conditions we find that the Lorentz force exceeds the gravitational and drag forces only for grains located at and above the uppermost, dashed green line in figure 8.

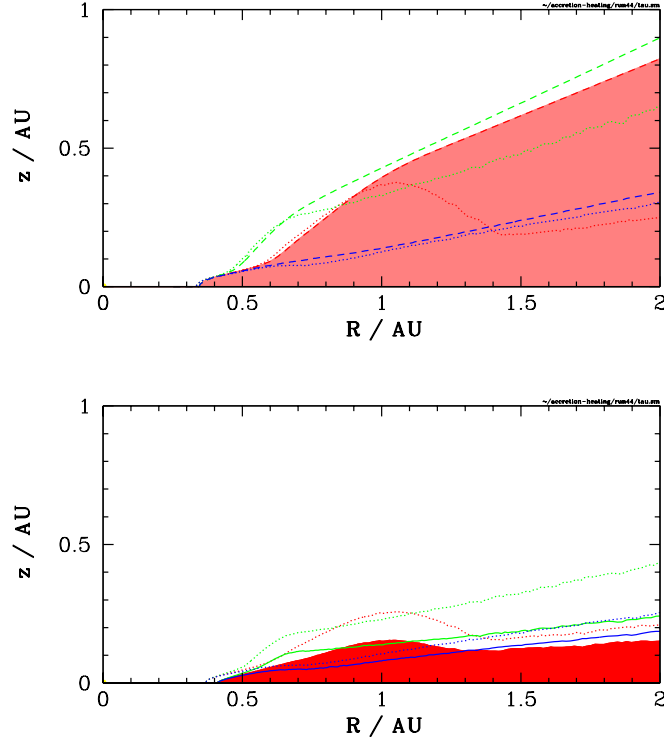


Fig. 8.— *Upper panel:* Dotted lines mark the height above which the settling time is less than ten orbits for 0.1- μ m grains in the three dusty disks. The dashed lines show the starlight-absorbing surface with the grains well-mixed, and are reproduced from figure 4 middle panel. The disk with gas support only is blue, with magnetic support throughout is green and with the magnetically-supported bump is the red line and shading. In all three cases, settling can lower the starlight-absorbing surface only slightly. *Lower panel:* Corresponding settling surfaces for 1- μ m grains (dotted), together with the unit vertical optical depth surfaces for thermal infrared emission (solid lines and shading). The same three dusty models appear in the same colors as in the upper panel. The settling line lies well above the infrared-emitting surface throughout, indicating settling is unimportant at the infrared photosphere.

9. SUMMARY AND CONCLUSIONS

Many young intermediate-mass stars show near-infrared excesses that have proven too large to explain using hydrostatic models. The hydrostatic disks are geometrically-thin near the silicate sublimation radius, intercepting and reprocessing too small a fraction of the starlight. On the other hand, MHD calculations indicate that magnetically-supported atmospheres are a generic feature of protostellar disk annuli undergoing accretion driven

by magneto-rotational turbulence. The MHD results show that magnetic forces suspend small amounts of material well above the hydrostatic photosphere. To see whether such an atmosphere can account for the excess near-infrared emission, we added simple exponential atmospheres to global models of the disk around a Herbig star. We placed the models jointly in vertical magnetohydrostatic balance and in radiative equilibrium with the starlight using Monte Carlo transfer calculations, and constructed synthetic observations of the resulting structures. Our main findings are that (1) the atmosphere near the sublimation radius is optically-thick to the starlight, and (2) if the dust abundance there is close to the interstellar value, the resulting near-infrared excess is sufficient to explain the median Herbig SED. We therefore suggest that magnetically-supported atmospheres are a common feature of at least the thermally-ionized inner annuli in Herbig disks.

Magnetically-supported disk atmospheres have several further interesting implications. First, the disk thickness measures not the temperature as long assumed, but the magnetic field strength. The gas pressure support yields only a lower bound on the height of the starlight-absorbing surface. The disk thickness is thus a gauge of the strength of the magnetic activity. Second, the disk atmosphere is quite diffuse. The exponential density profile falls off slower with height than the traditional Gaussian. The extended low-density atmosphere offers a natural explanation for the finding from interferometry, that the visibilities are better fit by hydrostatic disks combined with spherical or near-spherical halos than by either component alone. Kinematic diagnostics will be valuable in the future to help distinguish whether the extended material forms a turbulent magnetized atmosphere, an escaping wind, or perhaps most likely, both. Third, the inner disk’s atmosphere can throw a shadow across the material outside. A flared shape may bring the distant parts of the disk back up into the starlight. Dips in the radial surface brightness profile then do not have to be surface density deficits, but could be the shadows cast at sunset by magnetically-supported hills. Fourth, the atmosphere can obscure our view of the star even when the system is viewed at moderate inclination. Accounting for time-variable circumstellar extinction will be easier with magnetic fields holding some gas and dust aloft. In considering the consequences for the extinction, it is worth noting that we took a horizontally- and time-averaged atmospheric density profile, ignoring the structure that is universally part of magnetic activity in MRI turbulence as well as other contexts such as the Solar chromosphere.

We gratefully acknowledge discussions with C. Dominik, M. Flock, G. Mulders and A. Natta. The research was carried out in part at the Jet Propulsion Laboratory, California Institute of Technology, under a contract with the National Aeronautics and Space Administration and with the support of the NASA Origins of Solar Systems program via grant 11-OSS11-0074. NJT was also supported by the Alexander von Humboldt Foundation

through a Fellowship for Experienced Researchers. SH was supported by JSPS KAKENHI grants numbers 24540244 and 23340040. Copyright 2013 California Institute of Technology. Government sponsorship acknowledged.

REFERENCES

- Acke, B., Min, M., van den Ancker, M. E., Bouwman, J., Ochsendorf, B., Juhasz, A., & Waters, L. B. F. M. 2009, *A&A*, 502, L17
- Andrews, S. M., Wilner, D. J., Hughes, A. M., Qi, C., & Dullemond, C. P. 2010, *ApJ*, 723, 1241
- Armitage, P. J. 2011, *ARA&A*, 49, 195
- Bai, X.-N., & Goodman, J. 2009, *ApJ*, 701, 737
- Balbus, S. A., & Hawley, J. F. 1991, *ApJ*, 376, 214
- Bans, A., & Königl, A. 2012, *ApJ*, 758, 100
- Benisty, M., et al. 2010, *A&A*, 511, A74
- Bibo, E. A., & The, P. S. 1991, *A&AS*, 89, 319
- Bjorkman, J. E., & Wood, K. 2001, *ApJ*, 554, 615
- Chen, L., et al. 2012, *A&A*, 541, A104
- Dullemond, C. P., & Monnier, J. D. 2010, *ARA&A*, 48, 205
- Eisner, J. A., Chiang, E. I., Lane, B. F., & Akeson, R. L. 2007, *ApJ*, 657, 347
- Eisner, J. A., Lane, B. F., Hillenbrand, L. A., Akeson, R. L., & Sargent, A. I. 2004, *ApJ*, 613, 1049
- Eisner, J. A., et al. 2010, *ApJ*, 718, 774
- Flaig, M., Kley, W., & Kissmann, R. 2010, *MNRAS*, 409, 1297
- Fromang, S., & Papaloizou, J. 2006, *A&A*, 452, 751
- Furlan, E., et al. 2006, *ApJS*, 165, 568
- . 2009, *ApJ*, 703, 1964

- Gammie, C. F. 1996, *ApJ*, 457, 355
- Grinin, V. P., Arkharov, A. A., Barsunova, O. Y., Sergeev, S. G., & Tambovtseva, L. V. 2009, *Astronomy Letters*, 35, 114
- Grinin, V. P., Rostopchina, A. N., & Shakhovskoi, D. N. 1998, *Astronomy Letters*, 24, 802
- Hartmann, L., Calvet, N., Gullbring, E., & D’Alessio, P. 1998, *ApJ*, 495, 385
- Hartmann, L., Kenyon, S. J., & Calvet, N. 1993, *ApJ*, 407, 219
- Hillenbrand, L. A., Strom, S. E., Vrba, F. J., & Keene, J. 1992, *ApJ*, 397, 613
- Hirose, S., & Turner, N. J. 2011, *ApJ*, 732, L30+
- Isella, A., Tatulli, E., Natta, A., & Testi, L. 2008, *A&A*, 483, L13
- Kama, M., Min, M., & Dominik, C. 2009, *A&A*, 506, 1199
- Ke, T. T., Huang, H., & Lin, D. N. C. 2012, *ApJ*, 745, 60
- Kim, W.-T., & Ostriker, E. C. 2000, *ApJ*, 540, 372
- Lada, C. J., & Adams, F. C. 1992, *ApJ*, 393, 278
- Lucy, L. B. 1999, *A&A*, 344, 282
- Malfait, K., Bogaert, E., & Waelkens, C. 1998, *A&A*, 331, 211
- Manoj, P., Bhatt, H. C., Maheswar, G., & Muneer, S. 2006, *ApJ*, 653, 657
- Meijerink, R., Pontoppidan, K. M., Blake, G. A., Poelman, D. R., & Dullemond, C. P. 2009, *ApJ*, 704, 1471
- Mihalas, D. 1978, *Stellar atmospheres /2nd edition/* (San Francisco, W. H. Freeman and Co., 1978. 650 p.)
- Miller, K. A., & Stone, J. M. 2000, *ApJ*, 534, 398
- Monnier, J. D., et al. 2006, *ApJ*, 647, 444
- Mulders, G. D., & Dominik, C. 2012, *A&A*, 539, A9
- Natta, A., Grinin, V., & Mannings, V. 2000, *Protostars and Planets IV*, 559
- Okuzumi, S. 2009, *ApJ*, 698, 1122

- Okuzumi, S., & Hirose, S. 2011, *ApJ*, 742, 65
- Preibisch, T., Ossenkopf, V., Yorke, H. W., & Henning, T. 1993, *A&A*, 279, 577
- Thi, W.-F., Woitke, P., & Kamp, I. 2011, *MNRAS*, 412, 711
- Turner, N. J., Carballido, A., & Sano, T. 2010, *ApJ*, 708, 188
- Tuthill, P. G., Monnier, J. D., & Danchi, W. C. 2001, *Nature*, 409, 1012
- Umebayashi, T., & Nakano, T. 1988, *Progress of Theoretical Physics Supplement*, 96, 151
- van de Hulst, H. C. 1957, *Light Scattering by Small Particles* (New York: John Wiley & Sons)
- van den Ancker, M. E., de Winter, D., & Tjin A Djie, H. R. E. 1998, *A&A*, 330, 145
- Verhoeff, A. P., et al. 2011, *A&A*, 528, A91
- Vinković, D., Ivezić, Ž., Jurkić, T., & Elitzur, M. 2006, *ApJ*, 636, 348
- Vinković, D., & Jurkić, T. 2007, *ApJ*, 658, 462
- Yorke, H. W. 1986, in *Astrophysical Radiation Hydrodynamics*, ed. K.-H. A. Winkler & M. L. Norman, 141
- Zhu, Z., Hartmann, L., Gammie, C., & McKinney, J. C. 2009, *ApJ*, 701, 620